Structures 66 (2024) 106821

Contents lists available at ScienceDirect

Structures

journal homepage: www.elsevier.com/locate/structures

Topology optimization of vertical shear links in eccentrically braced frames

Yasser N. Saleh [a,b,*], Sherif A. Mourad [b], Amr M. Ibrahim [a]

[a] Civil Eng. Dept., Faculty of Engineering, British University in Egypt, 11837, Egypt
[b] Structural Eng. Dept., Faculty of Engineering, Cairo University, 12613, Egypt

ARTICLE INFO

Keywords:
Shear Links
EBF (Eccentrically Braced steel Frames)
Topology optimization
Cyclic loading

ABSTRACT

The inclusion of additive manufacturing (AM) in the construction industry has opened new perspectives on the production of structural members. By coupling AM technologies with topology optimization (TO), significant reductions in material usage and weight can be achieved. Although TO has been applied to optimize simply supported beams, additional factors such as stress concentrations, buckling, and low-cycle fatigue from seismic loads require further investigation. This study presents a numerical approach for optimizing shear links subjected to monotonic and cyclic loading. The numerical models for conventional shear links were validated against experimental work, including cyclic loading tests on individual shear links and scaled eccentrically braced frames (EBF). The implementation of TO led to a 12 % volume reduction in the first optimized link. The optimized link demonstrated superior performance, exhibiting higher shear strength and energy dissipation capacity under both monotonic and cyclic loading. Another study examined EBFs with vertical links, achieving 12 % and 30 % reduction in material volume. The optimized links showed improvements that reached 25 % compared to the conventional link in terms of strength and energy dissipation with 12 % volume reduction, while 30 % volume reduction showed slightly less improvement over EBFs with conventional shear links.

1. Introduction

With the emergence of additive manufacturing (AM) in the construction industry [1], manufacturing of topologically optimized structural members has become attainable. Topology optimization (TO) can reduce the weight of structural members while effectively achieving the serviceability and strength demand. Reduction in material usage can significantly influence the greenhouse gas emissions and energy consumptions [2]. The use of AM technology such as WAAM (Wire Arc Additive Manufacturing) coupled with TO for minimum weight can significantly benefit the environment [3]. The implementation of optimization algorithms can be used either to enhance the performance of structural systems [4–6] or members [7,8] in terms of strength and stiffness. Recently, several studies have focused on implementing TO on steel sections fabricated using WAAM. A novel approach has recently been introduced by Bruggi et al. [9] to incorporate the manufacturing constraints and the printing direction into TO algorithms for planar elements. This approach has been extended by Bruggi et al. [10] for I-shaped beams manufactured using WAAM method. Parts fabricated using WAAM can have an anisotropic behavior that is affected by the printing direction [11–13]. The extent of the anisotropic behavior is variable depending on the feedstock wire material as shown by Kessler and Sherman [14]. Bruggi et al. [10] compared the WAAM produced numerical models with conventional isotropic stainless steel (grade 304 L) beam models. Their study concluded that TO'ed beam elements with inclined build direction performed best, where up to 25 % weight reduction were achieved compared to conventional stainless steel. Furthermore, Mishra et al. [15] introduced a dynamic optimization algorithm where the printing direction changes at different locations depending on the load path. It was found that deposition directions aligned approximately at $\pm 45^{\circ}$ with the load-path result in significantly higher stiffness (up to 1.53 times) compared to the conventional approach where the deposition directions is set at a certain angle through the printing process.

The research findings from Bruggi et al. [10] were adopted by Laghi et al. [16] for the optimization of simply supported beams of IPE sections while constraining the deformation to a maximum of L/250. The material properties considered for the flanges corresponded to the 45° printing direction, while 0° printing direction material properties were used for the web. The results of the study presented in [16] concluded that TO beams were in compliance with the serviceability limits, while the study relied on numerical analysis only, the stress concentrations

* Corresponding author at: Civil Eng. Dept., Faculty of Engineering, British University in Egypt, 11837, Egypt.
E-mail addresses: Yasser.Nasr@bue.edu.eg (Y.N. Saleh), smourad@eng.cu.edu.eg (S.A. Mourad), amr.ibrahim@bue.edu.eg (A.M. Ibrahim).

https://doi.org/10.1016/j.istruc.2024.106821
Received 26 March 2024; Received in revised form 16 May 2024; Accepted 24 June 2024
Available online 28 June 2024

Table 1
Q345GJ material properties [26].

Parameter	σ^o (MPa)	C_1 (MPa)	γ_1	C_2 (MPa)	γ_2	C_3 (MPa)	γ_3	C_4 (MPa)	γ_4
Q345GJ	350	20 000	1000	10 000	100	600	20	350	10

and local buckling of compressed parts of the section should be further investigated.

One of the main drawbacks of using WAAM in the construction industry is mass production [17]. While TO'ed parts fabricated using WAAM technology may offer reduction in material usage and overall weight of the system [3], conventional techniques are still superior in terms of speed of manufacturing and production [17]. An alternative to the optimization of simple beams used to support floor decks, which are required in large numbers and fast delivery, the optimization of steel members for dissipative zones or seismic fuses such as shear links in eccentrically braced steel frames (EBF) becomes a more attractive option to study.

Shear links in EBF proved to be effective in energy dissipation resulted from seismic excitation since the introduction of EBF in the 1970s [18,19]. More recently, researchers have focused on studying and improving the energy dissipative capacity of links in EBF. Two recent studies investigated the flange contribution in the shear capacity of links [20,21]. Lazaro and Chacon [22] explored the use of austenitic stainless steel as an alternative material for the shear links, while steel grade S355 was used for the rest of the EBF framing members. Austenitic stainless steel, when subject to low cycle fatigue, provides considerable ductility and strain hardening [23,24], which is required for energy dissipative zones i.e., shear links. Lazaro and Chacon [22] were investigating the cyclic parameters influence on the behavior of EBF and the overstrength of the shear links. They extended their work and implemented their model for shear links on a five storey, single span EBF system adopted from [25]. A similar approach to the one adopted by [22] was also presented by Lian and Su [26] where steel grade Q345 was used for the links and high strength steel, grade Q455, was used for the other framing members in the EBF. Vertical shear links were proposed in the study as the behavior of test specimens were investigated against static pushover and dynamic shake table tests. The load carrying capacity of the frame of the EBF was still functioning even after the damage of vertical shear links. The seismic performance of the tested EBF system proposed by [26] was not superior when compared to conventional EBF systems manufactured using consistent material grade, however, in terms of overall weight of structural members, the proposed approach was better.

Liu et al. [27] proposed the use of Q345GJ steel for shear links. Q345GJ is the recommended material for design of steel structures in seismic zone as per the Chinese High-rise Steel Structure Specification. Consequently, 12 shear links with varying dimensions and stiffeners, while preserving a constant length were tested under cyclic loading in the study by [27]. The failure mode in all stiffened specimens was fracture in the web at the intersection with stiffeners along the welds while fracture between flange and endplate was observed for one specimen. The study [27] concluded that Q345GJ is ideal for shear links due to its ductility and capacity for low-cycle fatigue.

Ramonell and Chacon [28] introduced topology optimized horizontal EBF links. Their study included a wide range of European HEB steel sections while also varying the links' length. Nevertheless, in practical applications, shorter links are preferred for their higher deformation capacity and larger stiffness unless special architectural constraints exist [29,30]. Ramonell and Chacon [28] showed that shear optimized links provided higher strength but lower ductility compared to regular sections, while longer (flexural) optimized links were superior in both the ductility and strength compared to their conventional counterparts. Consequently, TO'ed shear links did not provide significant energy dissipation capacity based on their findings while optimized flexural links were ideal for the study as strength, ductility and energy dissipation were all enhanced.

In continuation of the recent research efforts to optimize steel members for best performance while minimizing weight, this paper investigates the behavior of topology optimized shear links subjected to monotonic and cyclic reversible loading. Topology optimization algorithm is implemented to improve the performance of shear links in EBF while reducing the total volume of steel materials used. One of the main aims of this research is to provide solutions to reduce consumption of raw materials while leveraging the flexibility in design and erection of parts using AM, however, this study does not include the calculation of carbon footprint for the additive manufacturing versus conventional subtractive manufacturing. The shear links are optimized for maximum stiffness and maximum energy dissipation and compared to conventional steel sections. The optimization procedure is undertaken using Abaqus Topology Optimization Module (ATOM) [31]. Using numerical models, the study then explores the implementation of the proposed TO shear links in single-storey EBF subjected to monotonic and cyclic displacement at storey level in order to investigate the nonlinear behavior of the whole EBF system. The TO'ed shear links should also provide adequate ductility for systems in seismic zones.

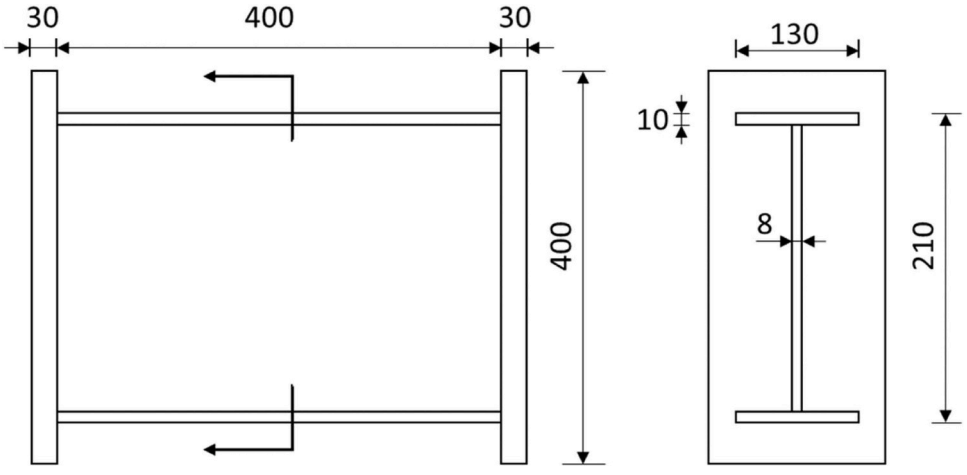

Fig. 1. Geometric properties of RSL-1 adopted from [27].

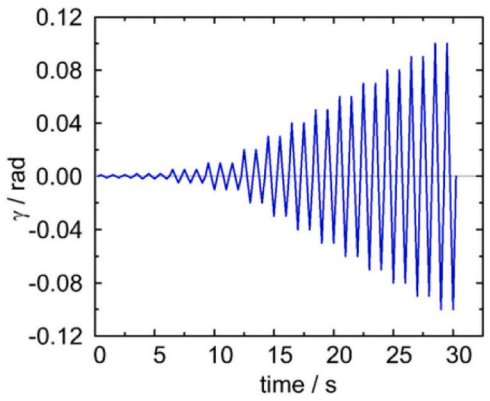

Fig. 2. Standard cyclic loading protocol provided by [27].

2. Material properties

In this research, shear links adopted from Liu et al. [27] are modelled and validated against the experimental results provided by the same source. The validation process is followed by a topology optimization process of shear links while the performance of the optimized part is compared against the conventional link under cyclic loading. Afterwards, in order to assess the performance of the optimized part in EBF systems, numerical validation of SDOF system adopted from [26] is carried out then the optimized parts are implemented for the EBF system.

Liu et al. [27] investigated the performance of shear links having a constant length (400 mm) while varying the cross-sectional properties and stiffeners' location. The reason this paper adopts the experimental work of [27] is that the cyclic behavior of the material Q345GJ was thoroughly and carefully studied to develop the constitutive model of Q345GJ steel. Their investigation concluded that Q345GJ steel provided good low-cycle fatigue capacity ideal for shear links and structural members prone to seismic loads. A summary of the parameters of the constitutive model is provided in Table 1, where σ^o represents the isotropic hardening yielding stress, γ_i represents the i^{th} kinematic hardening speed and C_i/γ_i represents the maximum value for the i^{th} kinematic hardening [32].

3. Numerical model

3.1. FE modelling and verification of shear links

A combined isotropic-kinematic hardening model is used for the material model where the parameters obtained from Table 1 are implemented. 8-node linear hexahedral elements (C3D8) were used with a mesh size of 5 × 5 mm. Tie constraints were used at the location of the welds without detailed modelling of the weld behavior or fracture as the main aim of the study is to obtain an optimized shape of the shear link depending on the behavior of the steel section. Detailed numerical modeling of the welds will add computational cost with little to no benefit to the optimization study. The cyclic loading protocol applied to the numerical model is corresponding to the standard load case provided by [27] and illustrated in Fig. 2.

The failure mode occurred in the experimental work of [27] was web fracture along the welds at the intersection of flanges and web which occurred after the 26th cycle (36 mm lateral displacement). Consequently, the numerical simulation only considered 26 cycles since no weld fracture is accounted for in the model. This assumption limits the comparisons made through cyclic testing in this study to the plastic deformation of links, assuming that all links would withstand at least 26 cycles before fracture of welds take place. A comparison between the deformed shape of the numerical versus the experimental work is provided in Fig. 3 at lateral displacement of 28 mm. Moreover, the shear force versus lateral drift (%) for the numerical model is provided in Fig. 4. The cyclic envelope (skeleton curve) of the hysteresis loops is plotted against the numerical model and it can be noticed that the numerical model is in good agreement with the data obtained from experimental testing with minor deviations as the numerical model recorded 2.5 % higher maximum shear force.

3.2. FE modelling and verification of EBF

Su and Lian [26] tested single-storey and 3-storey EBF systems for their study. This research focuses on the single-storey setup for the validation of the numerical model. The section properties are presented in Fig. 5, while the material properties can be shown in Table 2. Bilinear material models were adopted based on the data provided by [26] and presented in Table 2. The EBF was modelled twice, the first model is illustrated in Fig. 6 where 8-node linear hexahedral elements (C3D8) were used for link, beam and columns, while 10-node quadratic tetrahedron elements (C3D10) were used for the bracing due to the challenging geometries at the connection with the columns and the link.

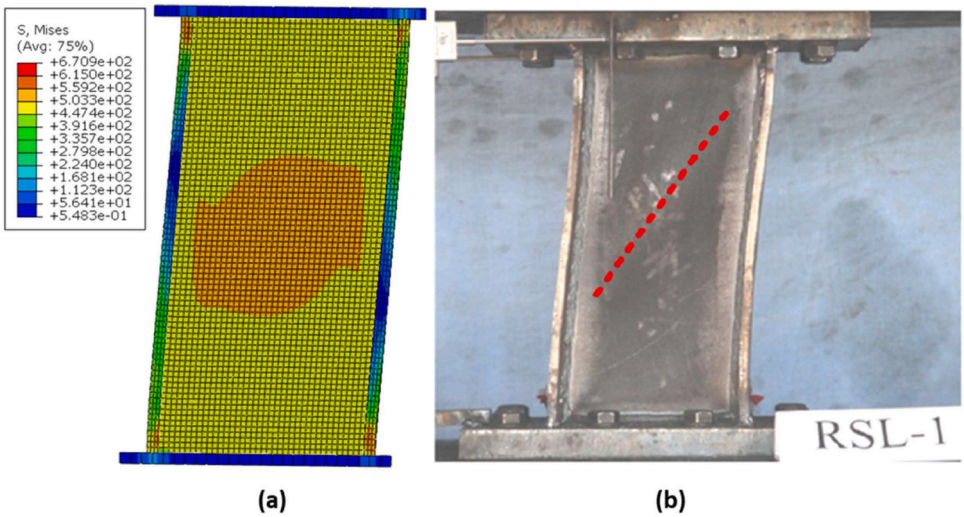

Fig. 3. Deformation at 28 mm lateral displacement (a) numerical (b) experimental [27].

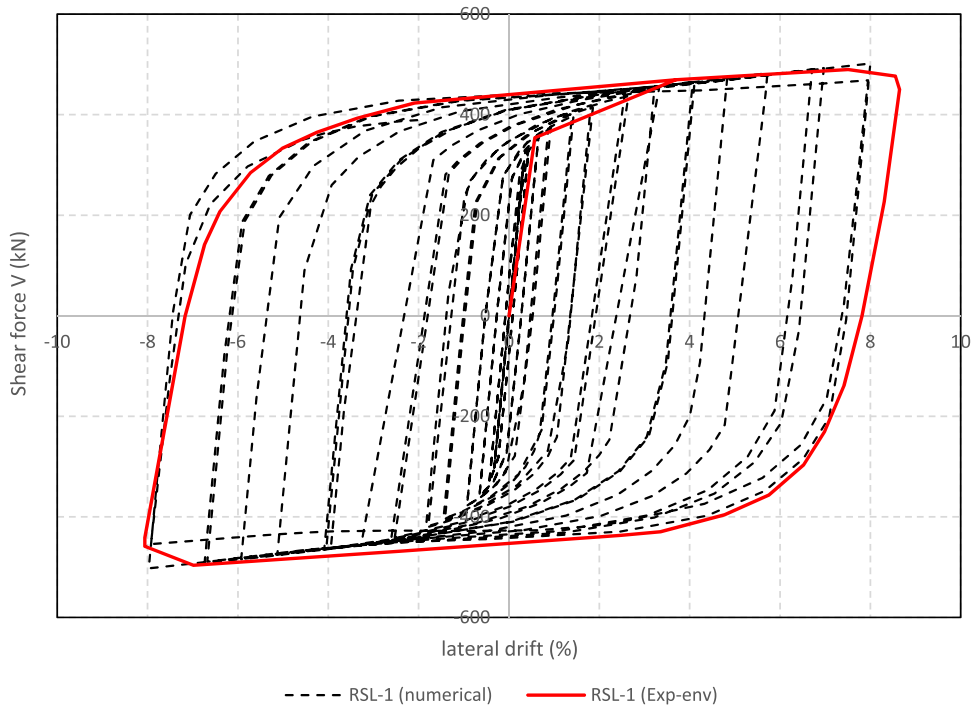

Fig. 4. Hysteresis loops from the numerical model (this study) vs. cyclic envelope (experimental) ↱[27].

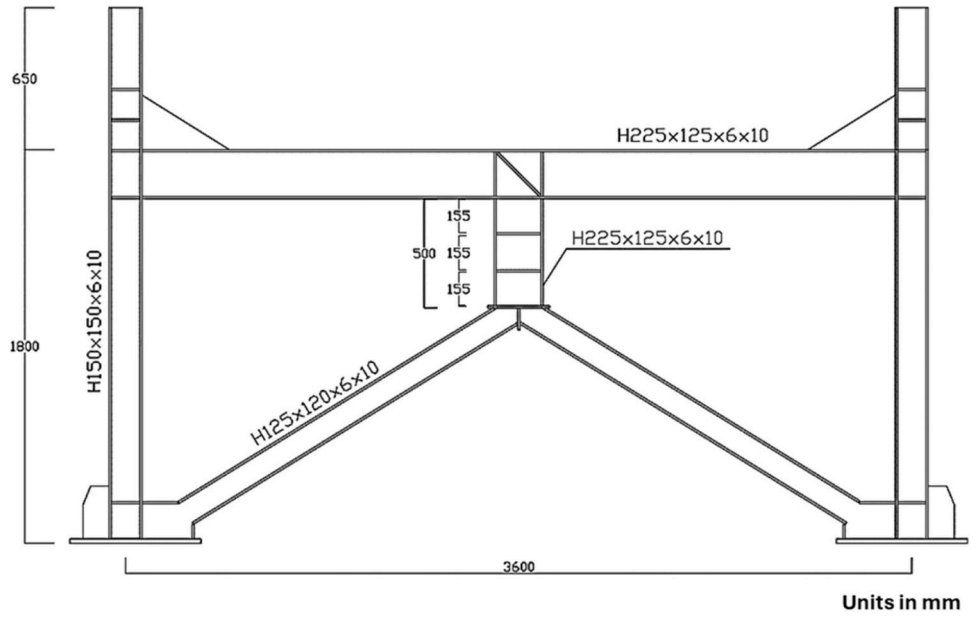

Fig. 5. Frame setup adopted from ↱[26].

Table 2
Material Properties for structural members in the EBF ↱[26].

Structural member	Links	Braces	Beams	Columns
Steel grade designation	**Q345**	**Q460**	**Q460**	**Q460**
f_y web	427.4	496.9	496.9	496.9
f_y flange	383.33	468.77	468.77	468.77
f_u web	571.1	658.57	658.57	658.57
f_u flange	554.4	627.97	627.97	627.97
Web elongation %	26.53	29.73	29.73	29.73
Flange elongation %	31.01	35.88	35.88	35.88

After a mesh sensitivity analysis, finer mesh size was used for the link as noticed in Fig. 6(c), where a mesh size of 10 × 10 mm was used. The mesh size for columns and bracing were 20 × 20 mm. Contact between all sections with each other at their ends was modelled using tie constraint such that no detailed modelling of weld behavior is implemented in the model.

In order to reduce the computational cost, another model was developed for the same problem while replacing bracings modelled using C3D10 elements with beam elements (B32), as kinematic coupling between the brace ends and the surfaces of the plates of the connection are applied, constraining translational DOFs, illustrated in Fig. 7. Static pushover load is applied, and the results are compared to the

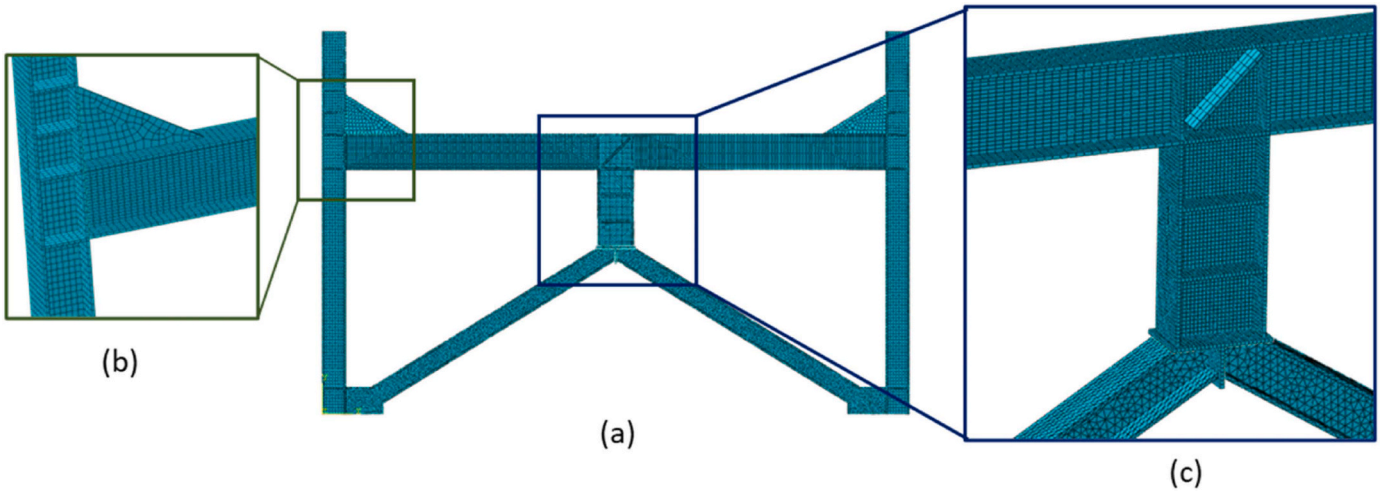

Fig. 6. (a) FE model of the single storey EBF (b) beam-column connection (c) shear link connection.

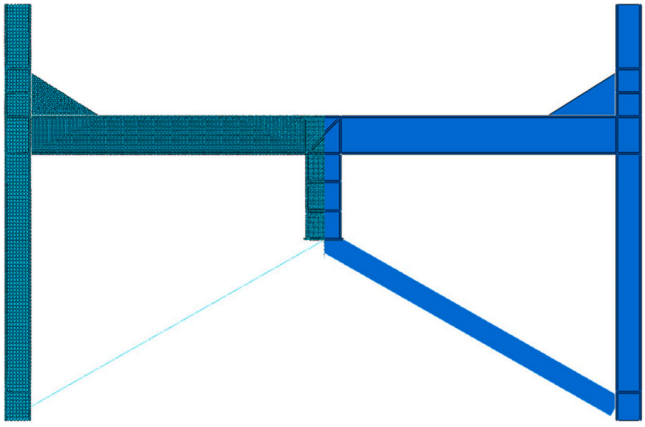

Fig. 7. Simplified FE model for the EBF.

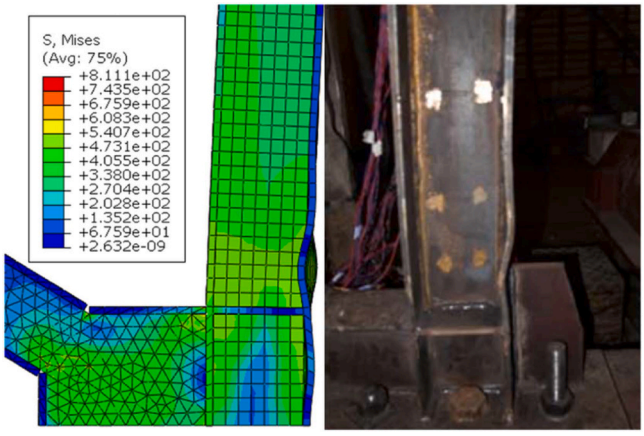

Fig. 9. Buckling of column flange at base connection.

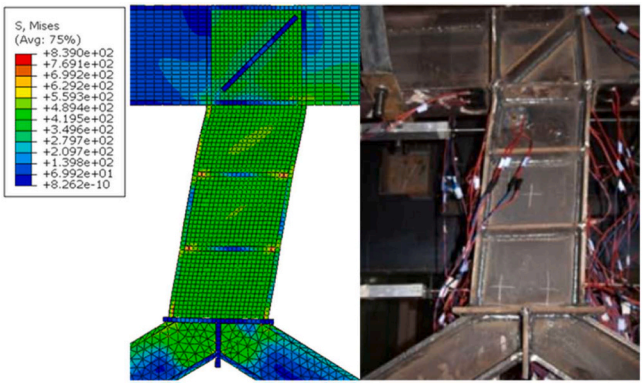

Fig. 8. Deformed shape of the shear link.

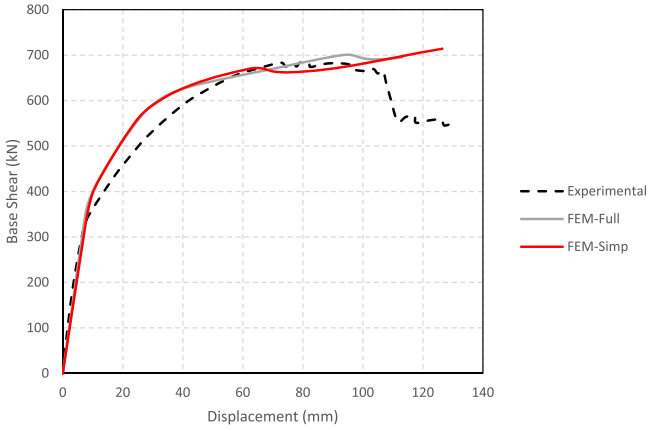

Fig. 10. Results of experimental [26] vs. numerical models of the one-storey EBF system.

experimental output.

Deformations at different locations on the EBF are compared to the FE model illustrated in Fig. 8 and Fig. 9. The base shear versus the frame lateral displacement curves are provided in Fig. 10. Yielding in the FE models was recorded at a value of 394 kN, which is 14 % higher than yield force (346 kN) recorded from the experimental test. For the post-yield behavior, the FE models were in good agreement with the experiment whether in terms of the post-yielding stiffness or deformation. The limitation of the FE models was the prediction of weld failure. Modelling of welds was not explicitly included in the model, instead, tie constraints were used. This explains the increasing trend in the curves of the FE models while a sudden drop in load-bearing capacity can be noticed for the experimental curve due to failure at welds. It can also be noticed that the simplified FE model was capable of predicting the behavior of the EBF almost as good as the full model while being significantly

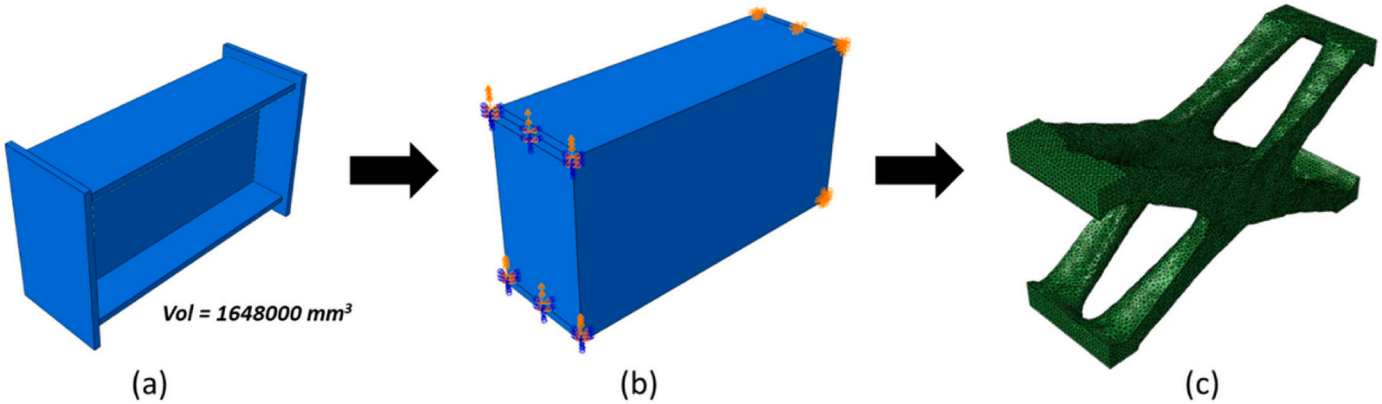

Fig. 11. Stages of optimization (a) source I-section (RSL-1) (b) optimization design space (c) optimized shape from ATOM.

computationally more efficient. Therefore, modelling of the bracing as beam elements (B32) is adopted for this research.

4. Optimization, results and analysis

4.1. Topology optimization algorithm

General (sensitivity-based) algorithm [33] is used for the optimization process of the shear link using Abaqus Topology Optimization Module (ATOM) where minimum compliance problem is formulated for the optimization process of the link. The compliance problem stipulates that maximum stiffness for the design domain can be achieved by minimizing the work done by external loads. This is achieved by minimizing the sum of strain energy of all discretized elements of the design domain, as indicated in (Eq. 1):

$$\min_{u,E_e} : c = U^T K U = \sum_{e=1}^{N} \quad u_e^T \quad k_0(E_e) \quad u_e \tag{1}$$

Where u_e is the displacement vector for individual element (e= 1,2,3 …. N), k is the stiffness matrix for element "e", which is a function of Young's modulus for an element with intermediate density, described in (Eq. 2):

$$E = \rho^p E_0 \tag{2}$$

Where ρ is the element relative density factor, p is the penalty factor that defines the effect of the density on the model stiffness, and E_0 is the Young's modulus of the fully solid material. This approach of penalized, proportional stiffness model has proven to be very efficient and popular in optimization problems that yields designs consisting of regions of material and no material, which is called the SIMP (Solid Isotropic Material with Penalization) material interpolation scheme [34]. The SIMP method is adopted with penalty factor (p) equals to 3 [35]. The stiffness of the whole model is then defined by (Eq. 3):

$$K_\rho = \sum_{e=1}^{N} \left[\rho_{\min} + (1-\rho_{\min})\rho_e^p\right] K_e \tag{3}$$

Where K_ρ is the modulated global stiffness, $\rho_{\min}$ is the minimum relative density (kept at 0.001), ρ_e is the element relative density factor, K_e is the element stiffness matrix and N is the number of discretized elements in the design domain. The design domain was created as a solid rectangular beam with the same depth, width and length as the original I-section (RSL-1). This design domain is subject to a volume constraint such that the volume of the final shape does not exceed that of RSL-1. Consequently, this approach should maximize the stiffness of the link given that the optimized link will have a volume equal to or less than the original shear link. It is reasonable to consider linear analysis during the optimization process since maximizing the stiffness of the link in the elastic range would also increase the stiffness of the link when large deformations are applied to it.

4.2. Topology optimization of shear links

Fig. 11 and Fig. 12 illustrate the workflow of the optimization process of the shear link. This workflow is recommended by recent guides on design for additive manufacturing (DfAM) [36]. Fig. 11(a) provides the geometry of RSL-1 shear link which is converted to a fully solid section with the same dimensions as illustrated in Fig. 11(b). Fixed boundary conditions are applied to the fully solid section at its tips at

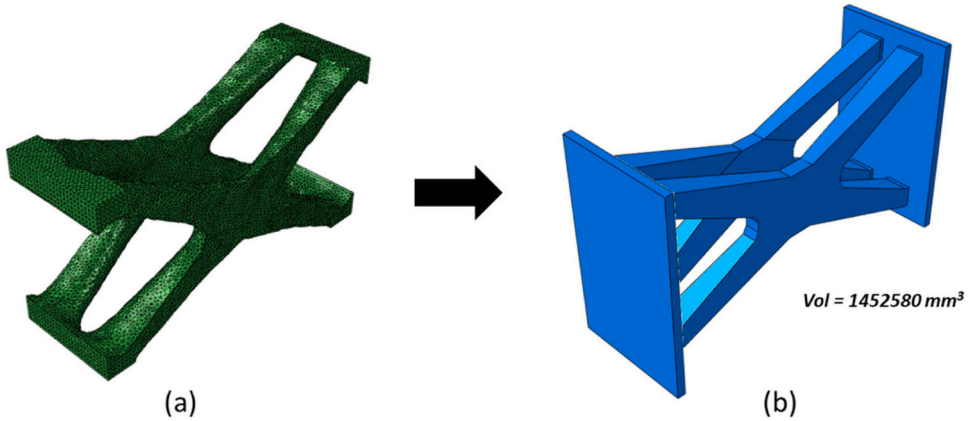

Fig. 12. (a) Raw optimized shape versus (b) final simplified shape after post-processing.

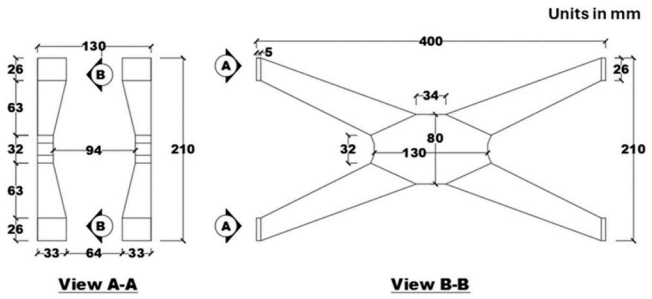

Fig. 13. Dimensions of the final simplified shape.

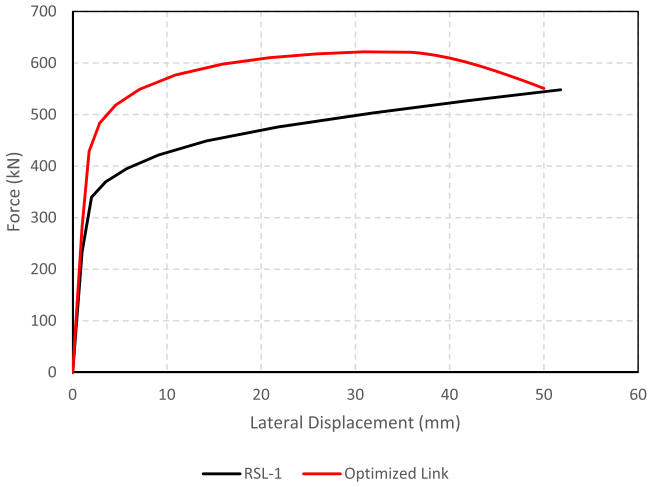

Fig. 14. Load-displacement curves for monotonic displacement of RSL-1 and optimized shear links.

one end while displacement is applied at the other end. For computational efficiency, linear elastic analysis was considered for the optimization process which yielded the optimized shape provided in Fig. 11(c) after 26 design cycles. It can be noticed that the TO algorithm resulted in an optimized shape that adapts to the shear stress by resisting its tension and compression stress components.

The optimized shape is further processed to obtain a more simplified shape that can be useful for 3D printing in future work, illustrated in Fig. 12 and Fig. 13. The final simplified shape is obtained by measuring distances at different locations on the raw optimized shape. Fig. 12(b) illustrates the final optimized shape after post-processing. The final optimized shape had a 12 % reduction in volume compared to RSL-1.

To compare the performance of the optimized link versus RSL-1, both links are subjected to monotonic pushover lateral movement and quasi-static cyclic loading. Fig. 14 provides a plot of the load-displacement curves for both links subject to monotonic displacement. The simulation is stopped at 50 mm lateral displacement since the experimental tests indicated that fracture of welds occurred for RSL-1 at displacement equals 36 mm when subjected cyclic load. Fig. 14 shows that the optimized link had a maximum shear resistance of 622 kN, which is 13.5 % than RSL-1. If only 36 mm displacement is considered, the difference increases to 20 % indicating that the optimization process achieved higher shear resistance with less material (volume). The deformed shape of the optimized link is provided in Fig. 15. It can be noticed that the failure mode of the optimized link differs significantly from the conventional shear link where shear buckling of the web takes place.

Fig. 16 provides the hysteresis loops for both RSL-1 and optimized links, while Fig. 17 highlights their corresponding cyclic envelopes. The

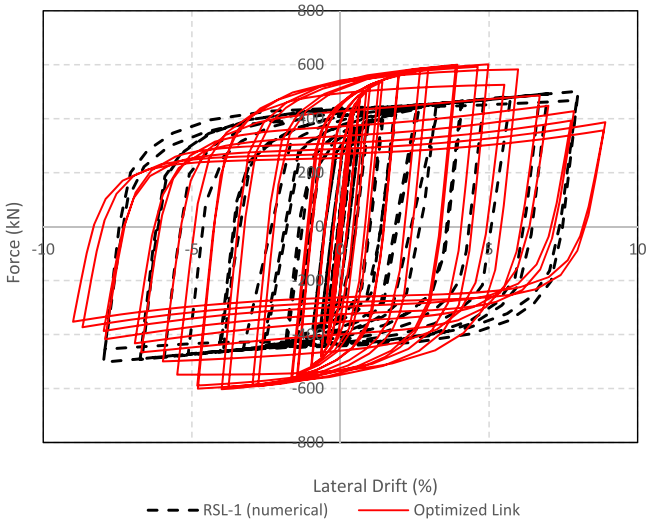

Fig. 16. Load-displacement curves for cyclic loading of RSL-1 and optimized shear links.

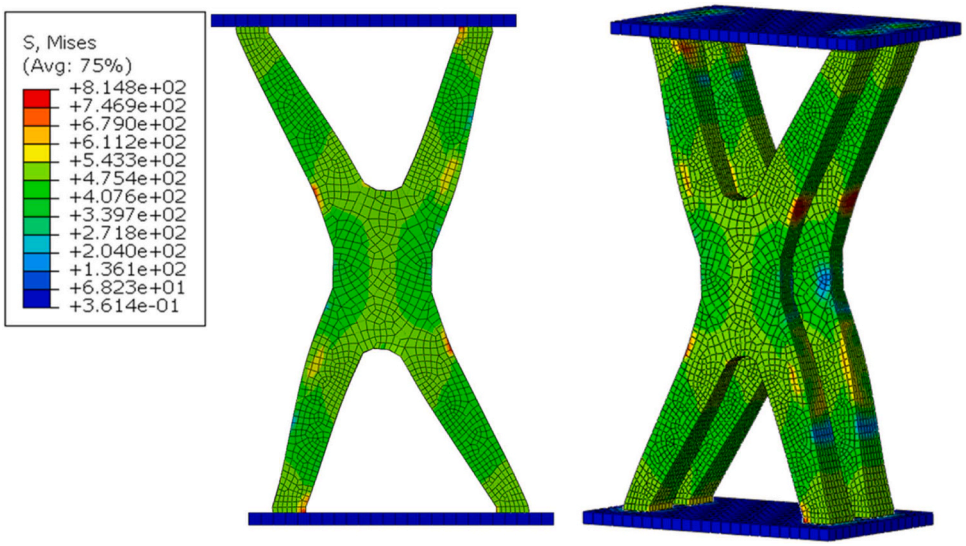

Fig. 15. Deformed shape of the optimized link.

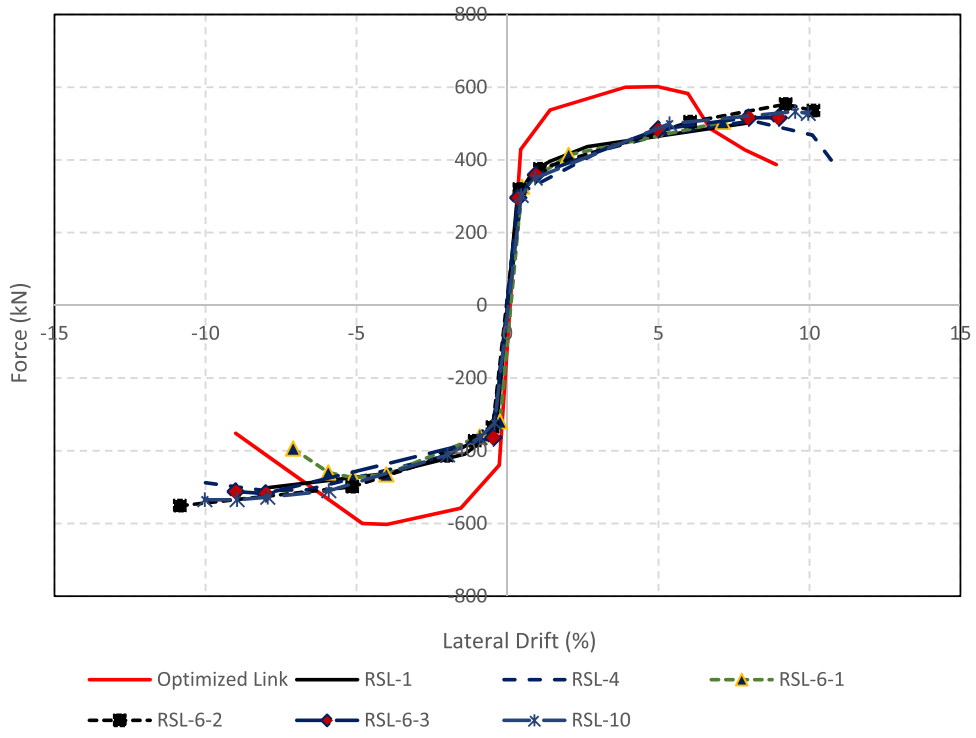

Fig. 17. Cyclic envelope of different RSL links versus optimized shear link.

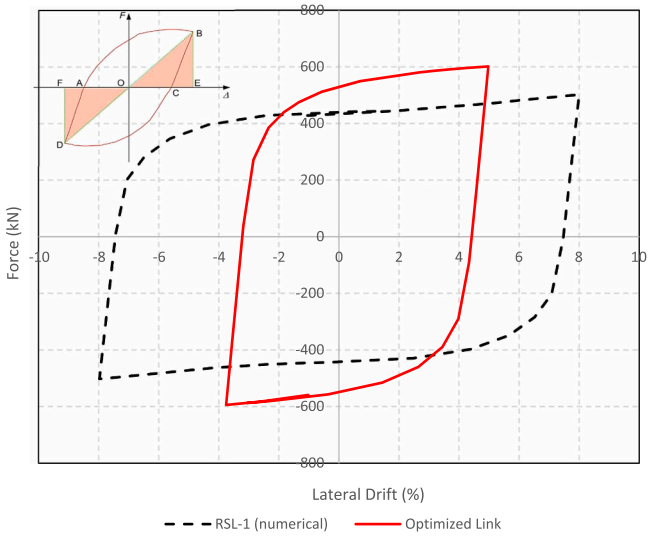

Fig. 18. Cycles used for calculation of damping coefficient.

highest shear force recorded for the optimized shape is 601 kN, which is 20 % higher than RSL-1 (502 kN). Moreover, the intended use of shear links in structures prone to seismic loading is to dissipate energy, consequently, the energy dissipation capacity and the equivalent viscous damping coefficients are calculated to compare the performance of both links. The energy dissipated during cyclic loading is calculated as the area under the cyclic envelope curve. It was found that the optimized link provided 31 % increase in the energy dissipation capacity compared to RSL-1 marking a significant seismic performance enhancement.

Another measure of the energy dissipative capacity is the equivalent damping coefficient, h_e defined by Eq. (3) and illustrated in Fig. 18 [37]:

Table 3
Summary of comparison between RSL-1 and optimized link.

		RSL-1	Optimized Link	Diff (%)
Monotonic	Max. V (kN) (50 mm disp)	548	622	13.4
	Max. V (kN) (36 mm disp)	514.8	621.816	20.8
Cyclic	Max. V (kN)	502	601	19.9
	Energy Dissipation (J)	27522	32659	31
	Damping Coefficient	0.55	0.56	2.0

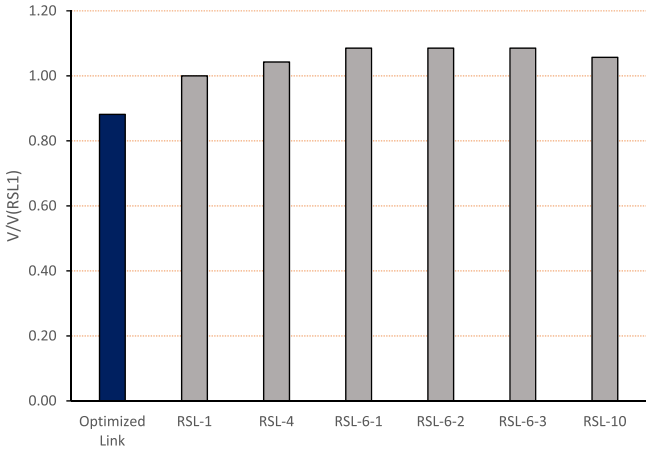

Fig. 19. Illustration of volume reduction of the optimized link compared to RSL links.

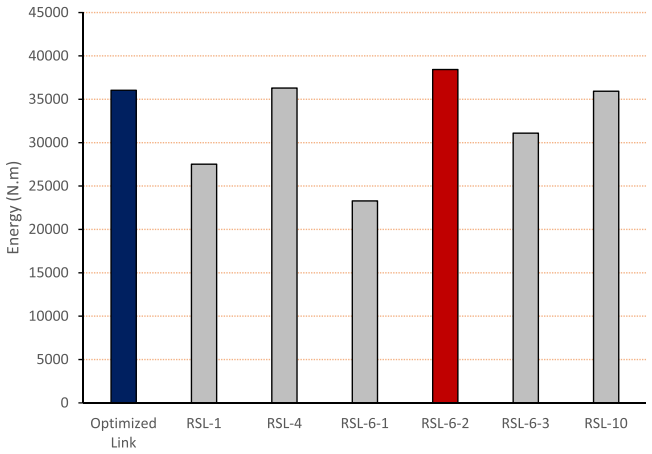

Fig. 20. Energy dissipated calculated from the cyclic envelope (skeleton) curves.

$$h_e = \frac{1}{2\pi}\cdot\frac{S_{ABC}+S_{ADC}}{S_{BOE}+S_{DOF}}\# \quad (3')$$

The term $S_{ABC}+S_{ADC}$ resembles the energy dissipated during one complete cycle, while $S_{BOE}+S_{DOF}$ represents the total strain energy assuming the link behaves elastically until reaching the target displacement. The damping coefficient is calculated from the cycle that resulted in the maximum recorded shear resistance (points B and D) as illustrated in Fig. 18. It was found that the damping coefficient for both links were almost identical. A summary of results obtained for the comparison is provided in Table 3.

Fig. 17 also provides the cyclic envelope curves for different I-shaped RSL shear links extracted from ↱[27] having the same cross-sectional dimensions and link length but with added stiffeners. These added stiffeners resulted in additional material used, consequently, Fig. 19 presents the volume of links relative to RSL-1. RSL-6–2 had the best performance in terms of shear resistance, energy dissipation and ductility compared to other RSL links while increasing the volume of the link by 10 %, as illustrated in Fig. 19 and Fig. 20. When RSL-6–2 is compared to the optimized link, the latter exceeds the former by 12 % in shear resistance with 20 % less material, however, RSL-6–2 had 6 % higher energy dissipated during cyclic loading. Other than RSL-6–2, the optimized link exceeded the RSL shear links in shear strength or energy dissipated with less material.

4.3. Implementation of optimized link in EBF

In order to assess the behavior of the optimized link in EBF systems, the optimized shape for the link is implemented in the EBF frame as shown in Fig. 21. Two optimized links were proposed having different volume reductions, one with 12 % volume reduction as obtained from the shear link study, then a more aggressive reduction in material was pursued for the second link with 30 % reduction in volume. Moreover, the original shear link had different material properties for the web and flanges as indicated in Table 2 and since the optimized links have a solid homogeneous shape, the links were modelled once using the material

Table 4
Naming convention for the FE models.

Link ID	Description
Opt-12 %-W	The EBF model where optimized link of 12 % volume reduction is used, having the material model of the original shear link's web
Opt-12 %-F	Optimized Link, 12 % volume reduction, Flange material model
Opt-30 %-W	Optimized Link, 30 % volume reduction, Web material model
Opt-30 %-F	Optimized Link, 30 % volume reduction, Flange material model

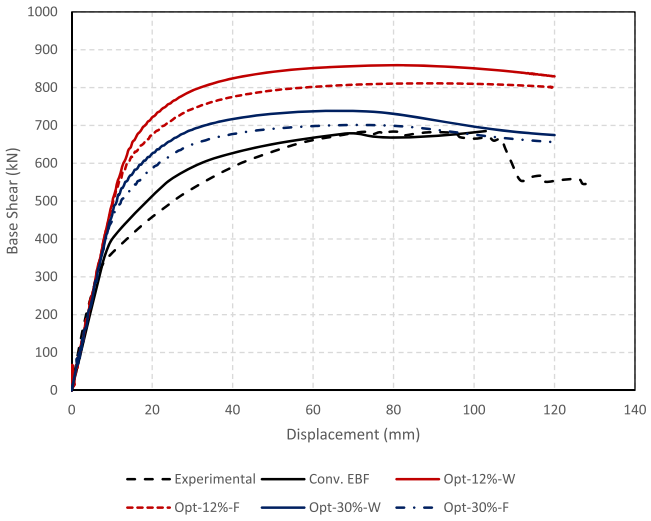

Fig. 22. Base shear versus lateral displacement curves.

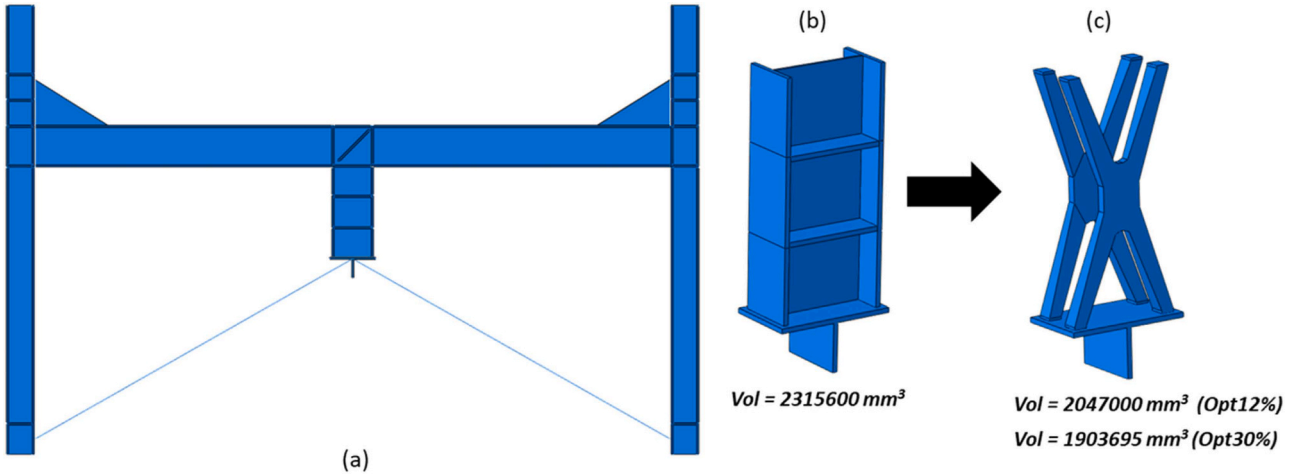

Fig. 21. (a) Illustration of the EBF (b) shear link from ↱[26] (c) optimized link to replace the existing link.

Table 5
Sequence of plastic deformations observed for EBF.

Model ID	Sequence of elements entering plastic stage			
EBF with conventional link	(1) Δ= 4.2 mm P = 185.1 kN Yielding initiated @ Opt. link's web S_{mises} > 427 MPa	(2) Δ= 6.9 mm P = 302.58 kN Beam's web @panel zone above link started to yield Smises > 497 MPa	(3) Δ= 55.56 mm P = 660.5 kN Buckling Occurred at link Web and flange Fig. 8	(4) Δ= 73.7 mm P = 672.6 kN Buckling Occurred at Column Base Fig. 9
Opt-12 %-W	(1) Δ= 3.62 mm P = 188.2 kN Yielding initiated @ Opt. link S_{mises} > 427 MPa	(2) Δ= 11.53 mm P = 556.8 kN Beam's web @panel zone above link started to yield S_{mises} > 497 MPa	(3) Δ= 31.1 mm P = 796.5 kN Flange buckling Occurred at Column Base	(4) Δ= 43.97 mm P = 832.2 kN Column panel zone yielded and column flange buckled below the panel zone
Opt-12 %-F	(1) Δ= 7.95 mm P = 396.5 kN Yielding initiated @ Opt. link S_{mises} > 383 MPa	(2) Δ= 11.98 mm P = 558.1 kN Beam's web @panel zone above link started to yield S_{mises} > 497 MPa	(3) Δ= 23 mm P = 699.8 kN Flange buckling Occurred at Column Base	(4) Δ= 39 mm P = 773.4 kN Column panel zone yielded and column flange buckled below the panel zone
Opt-30 %-W	(1) Δ= 9.1 mm P = 431 kN Yielding initiated @ Opt. link S_{mises} > 427 MPa	(2) Δ= 33.6 mm P = 701.3 kN Flange buckling Occurred at Column Base		(3) Δ= 41.4 mm P = 719.4 kN Column panel zone yielded and column flange buckled below the panel zone
Opt-30 %-F	(1) Δ= 8.75 mm P = 407.8 kN Yielding initiated @ Opt. link S_{mises} > 427 MPa	(2) Δ= 32.3 mm P = 658 kN Flange buckling Occurred at Column Base		(3) Δ= 39 mm P = 675 kN Column panel zone yielded and column flange buckled below the panel zone

*S_{mises} is obtained at the centroid of the C3D8 solid elements of the mentioned zone of each stage.

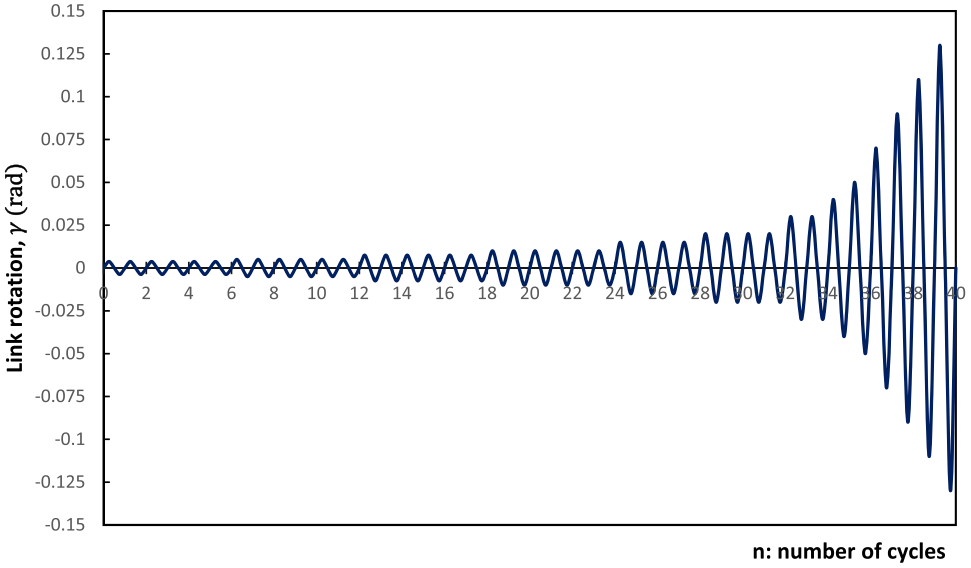

Fig. 24. AISC 341–16 loading sequence [22].

model used for the web of the original shear link and once using the flange properties. The naming convention for the models are provided in Table 4.

4.3.1. Monotonic quasi-static pushover analysis

A monotonic displacement is applied to the EBF and the base shear versus lateral displacement is plotted and shown in Fig. 22. It is found that Opt-12 %-W and Opt-12 %-F reached 26 % and 19 % higher base shear compared to the conventional EBF, respectively. The increase in base shear indicates an increase in the stiffness of the EBF. These differences were originally the main drive to investigate the performance of shear links with higher volume reduction. Opt-30 %-W and Opt-30 %-F had a slightly higher baser shear reaching 8 % and 3 % higher base shear over the conventional EBF, respectively.

An important aspect of quasi-static pushover analysis is observing the behavior of the EBF at various locations, aside from the dissipative shear links. It is crucial to ensure that these links yield before the columns and beams do. In all models, the dissipative shear links yielded first, which is an essential phenomenon to ensure ductility of the EBF when subjected to seismic loads. Large plastic deformations and buckling at column base took place at higher lateral displacement of the EBF when conventional link was used, however, the maximum base shear

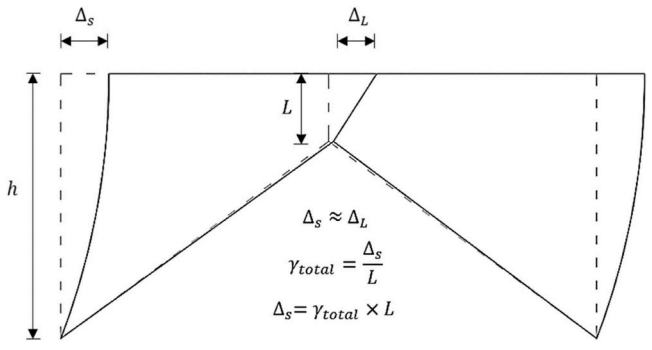

Fig. 25. Illustration of converting link rotation to lateral displacement.

withstood was the lowest compared to other optimized links systems. The following Table 5 summarizes the observed stages of plasticity obtained from the numerical models.

4.3.2. Quasi-static cyclic loading analysis

The performance of the links is then assessed under cyclic loading where the loading protocol follows the AISC 341–16 loading sequence [38] illustrated in Fig. 24. Moreover, Fig. 25 expands on converting the link rotation to storey displacements applied to the EBF. This approach is adopted since the monotonic pushover test has shown that the stiffness of the beam is high enough to assume the deformed shape provided in Fig. 25.

Fig. 26 provides the hysteresis loops for EBF with the conventional link versus all EBFs with optimized links, while Fig. 27 features their respective cyclic envelopes. It can be noticed that Opt-12 %-W had the highest stiffness with maximum base shear of 887 kN, 30 % higher than the conventional EBF. Opt-12 %-F had slightly less stiffness with maximum base shear equals 853.5 kN, 25 % higher than the conventional EBF. Opt-30 %-W and Opt-30 %-F had almost the same maximum base shear when to conventional EBF. Comparing the post-yield behavior of the models, it can be noticed that the EBF with conventional link exhibited cyclic strain hardening with increased resistance to deformation. All Opt. models exhibited similar post-yield behavior where cyclic strain hardening is followed by cyclic strain softening. Opt-30 %-W and Opt-30 %-F exhibited cyclic hardening behavior until reaching a displacement of + 38 mm and + 37.6 mm, respectively, then large plastic deformations and buckling of flanges at columns base are initiated. Similarly, Opt-12 %-W and Opt-12 %-F exhibited cyclic hardening behavior until reaching a displacement of + 48 mm and + 54.4 mm, respectively, where buckling of flanges at columns base took place. The energy dissipation calculated from the cyclic envelope curve indicates that the optimized links also outperformed the conventional EBF. Opt-12 %-W achieved 26 % higher energy dissipation while Opt-12 %-F was 12 % higher. Opt-30 %-W and Opt-30 %-F were also close to the conventional EBF in terms of energy dissipation. Nevertheless, it can be noticed that the hysteresis loops obtained from the cyclic loading of the conventional EBF had more plumpness when compared to EBFs with optimized links indicating higher energy dissipative capabilities. The damping coefficient calculated from Eq. (3) can translate the plumpness of the curves numerically.

A summary of the results obtained from the monotonic and cyclic tests is provided in Table 6 including the damping coefficients for all models. The conventional link outperformed all optimized links in the damping coefficient parameter, which translates to a ratio of $D/D_{cov.}$ less than 1. This can be attributed to the deformation and failure mode of the links. In the optimized shear links models of the EBF, the redistribution of material from the TO procedure resulted in thicker web with reduced surface area, as provided in Fig. 21(c)., mitigating the shear-buckling mode that is common in conventional shear links. The load-bearing behavior transitions from traditional shear mechanisms to more efficient tension-compression mechanisms simulating a strut-and-tie behavior, as illustrated in Fig. 23(b). Struts in the optimized links efficiently channel compressive forces along straight-line paths and reducing stress concentrations while ties, on the other hand, facilitate the transfer of tensile forces. This reorganization of internal forces enhances the strength and stiffness for the links. Nevertheless, conventional shear links showed efficient energy dissipation, represented in the damping coefficient parameter, depending on shear buckling of the web for energy dissipation, compared to the deformed shapes of optimized links where sudden drop in strength after buckling of the links at regions under compressive stress took place.

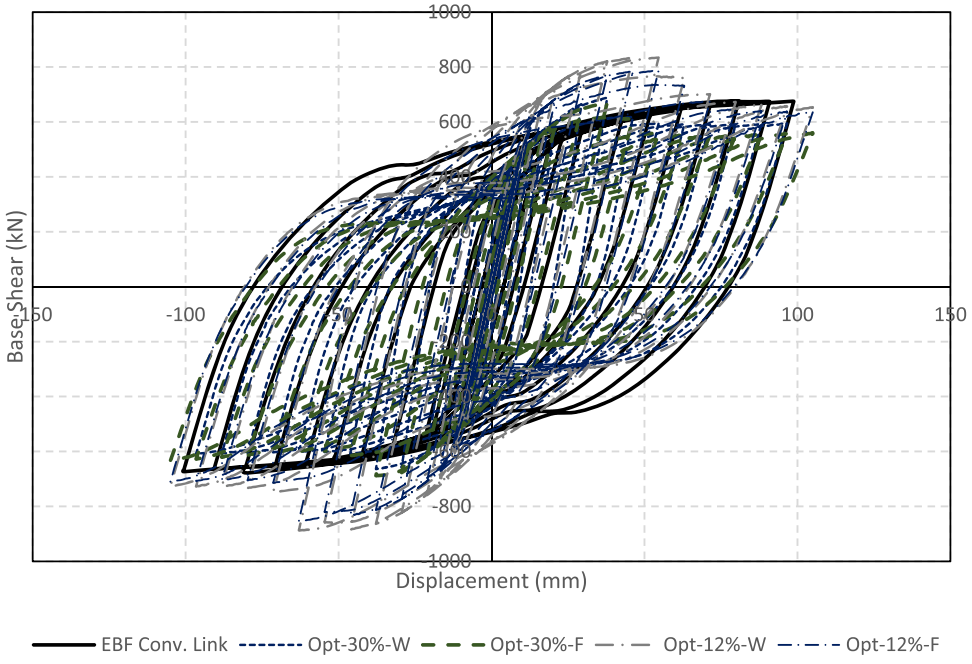

Fig. 26. Load-displacement curves for cyclic loading of EBF with I-section and optimized shear links.

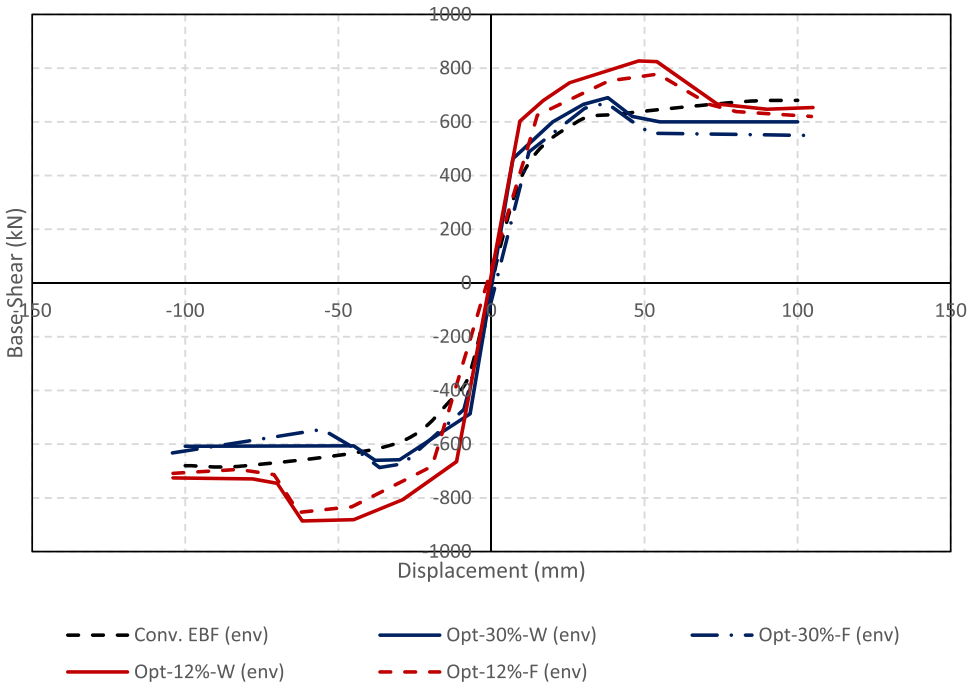

Fig. 27. Cyclic envelope of EBF with I-section and optimized shear links.

Table 6
Summary of comparison between EBF with I-section and optimized links.

Loading Type	Parameter	EBF - Conv. Link	Opt12 %-W	Opt12 %-F	Opt30 %-W	Opt30 %-F
Monotonic	$V/V_{conv.}$	1.00	1.26	1.19	1.08	1.03
Cyclic	Max. $V/V_{conv.}$	1.00	1.22	1.15	1.00	0.98
	Min. $V/V_{conv.}$	1.00	1.30	1.25	0.97	1.01
	*$E/E_{conv.}$	1.00	1.26	1.12	1.00	0.97
	**$D/D_{cov.}$	1.00	0.80	0.80	0.83	0.53

* E refers to energy dissipation, calculated from area under the cyclic envelope (skeleton) curve
** D refers to damping coefficient

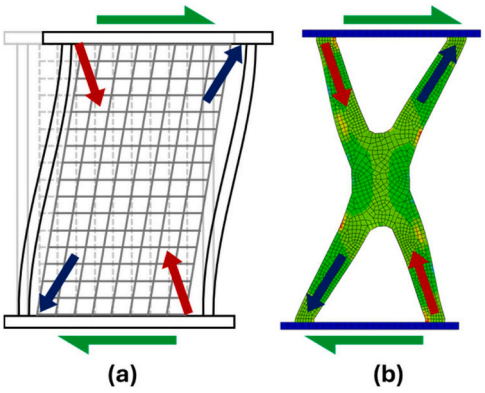

Fig. 23. (a)Shear buckling in conventional link versus (b)Strut and tie behavior of the optimized link.

5. Conclusions

Additive manufacturing (AM) has made it possible to manufacture topologically optimized structural members in the construction industry where AM technologies like WAAM coupled with TO can benefit the environment by reducing material usage. This paper provided a numerical approach for optimizing shear links subjected to monotonic and cyclic loading. Nonetheless, it is essential to highlight that this study focuses on the behavior of the shear links prior damage and fracture at welded joints. In addition, further analysis of optimized links with different dimensions for the design space can be investigated. Future research can also investigate the performance of optimized shear links in multi-storey structures subjected to quasi-static and dynamic loadings. The following points summarize the conclusions drawn from the optimization study:

a) The first optimized link was compared to the shear link designated as RSL-1 and achieved a volume reduction of 12 %. The optimized link proved to be superior in almost every aspect when its performance is compared to RSL-1.
b) The optimized link had shear strength that reached 20 % higher than RSL-1 when subjected to monotonic loading, in addition, the maximum shear force recorded for the optimized link under cyclic loading also reached 20 % higher than the conventional link. Moreover, the energy dissipation capacity of the optimized link calculated using the cyclic envelope was 19 % higher than RSL-1 while the damping coefficient was almost the same for both links.
c) The optimized link is compared to other experimentally tested RSL links. It was found that the optimized link also surpassed other RSL links in shear resistance and energy dissipation.
d) In order to expand on the performance of TO'ed shear links, another study that included testing of EBFs with vertical links was included. Optimized links with 12 % and 30 % reduction in material are investigated to assess the effect of reducing materials aggressively on the behavior of the links.

e) For Opt-12 % links, stiffness and energy dissipation were significantly increased reaching 30 % and 25 % respectively, when compared to EBF with conventional link. Nonetheless, the damping coefficient calculated for conventional links were higher compared to the optimized links, indicating that failure mechanisms of optimized links influence greatly the damping coefficient parameter.
f) For Opt-30 % links, the differences in strength and energy dissipation were much less when compared to the conventional link. The EBF with optimized link had 8 % higher base shear compared to I-shaped link, in addition, the performance was almost the same when cyclic loading is applied. The difference in maximum base shear recorded from the cyclic loading was less than 2 % while the energy dissipated, calculated from the cyclic envelope, was less than 1 %. The damping coefficient calculated for the I-shaped conventional link was 15 % higher than the optimized link which was also visible in the shape of the hysteresis loops.
g) Shear buckling of the web is expected for conventional I-shaped shear links, which is not the case for the optimized links. The failure mode for the optimized shapes is either buckling or tension failure at the straight segments of the link.

CRediT authorship contribution statement

Amr Mohamed Ibrahim: Writing – review & editing, Supervision, Conceptualization. **Yasser Nasr Saleh:** Writing – original draft, Visualization, Methodology, Investigation, Formal analysis. **Sherif A. Mourad:** Writing – review & editing, Supervision.

Declaration of Competing Interest

The authors declare that they have no known competing financial interests or personal relationships that could have appeared to influence the work reported in this paper.

Acknowlegement

The authors would like to acknowledge the British University in Egypt (BUE) for the support of this research.

References

[1] Kanyilmaz, A., Demir, A.G., Chierici, M., Berto, F., Gardner, L., Kandukuri, S.Y., & Razavi, N. (2022). Role of metal 3D printing to increase quality and resource-efficiency in the construction sector. Additive Manufacturing, 50, 102541. https://doi.org/10.1016/j.addma.2021.102541.
[2] Pomponi F, Moncaster A. Reducing embodied carbon in the built environment: a research agenda. Sustain Ecol Eng Des Soc (SEEDS) 2016;68. https://doi.org/10.17863/CAM.7354.
[3] Shah IH, Hadjipantelis N, Walter L, Myers RJ, Gardner L. Environmental life cycle assessment of wire arc additively manufactured steel structural components. J Clean Prod 2023;389:136071.
[4] Zhao B, Yi J, Jiang C, Lu X. Experimental study on seismic performance of super high-rise building with topology optimized diagonal mega frame. J Build Eng 2023:107003.
[5] Kyvelou P, Spinasa A, Gardner L. Testing and analysis of optimized wire arc additively manufactured steel trusses. J Struct Eng 2024;150(3):04024008. https://doi.org/10.1061/JSENDH.STENG-12832.
[6] Tsavdaridis KD, Nicolaou A, Mistry AD, Efthymiou E. Topology optimisation of lattice telecommunication tower and performance-based design considering wind and ice loads. Structures 2020;Vol. 27:2379–99. https://doi.org/10.1016/j.istruc.2020.08.010.
[7] Xu Y, Ma Z, Huang Q. Multi-constrained topology optimization of prefabricated joints in large-span latticed structures. Structures 2023;Vol. 56:104809. https://doi.org/10.1016/j.istruc.2023.06.140.
[8] Chiu LN, Rolfe B, Wu X, Yan W. Effect of stiffness anisotropy on topology optimisation of additively manufactured structures. Eng Struct 2018;171:842–8. https://doi.org/10.1016/j.engstruct.2018.05.083.
[9] Bruggi, M., Laghi, V., & Trombetti, T. (2021). Simultaneous design of the topology and the build orientation of Wire-and-Arc Additively Manufactured structural elements. Computers & Structures, 242, 106370.
[10] Bruggi M, Laghi V, Tomaso T. Optimal design of wire-and-arc additively manufactured i-beams for prescribed deflection. Comput Assist Methods Eng Sci 2022;24(4):357–78.
[11] Kyvelou P, Slack H, Mountanou DD, Wadee MA, Britton TB, Buchanan C, et al. Mechanical and microstructural testing of wire and arc additively manufactured sheet material. Mater Des 2020;192:108675.
[12] Laghi V, Palermo M, Tonelli L, Gasparini G, Ceschini L, Trombetti T. Tensile properties and microstructural features of 304L austenitic stainless steel produced by wire-and-arc additive manufacturing. Int J Adv Manuf Technol 2020;106:3693–705.
[13] Chen M-T, Zhang T, Gong Z, Zuo W, Wang Z, Zong L, et al. Mechanical properties and microstructure characteristics of wire arc additively manufactured high-strength steels. Eng Struct 2024;300:117092. https://doi.org/10.1016/j.engstruct.2023.117092.
[14] Kessler HD, Sherman RJ. Tension and charpy V-notch impact properties of wire arc additively manufactured ER80S-Ni1. Structures 2024;Vol. 61:106134. https://doi.org/10.1016/j.istruc.2024.106134.
[15] Mishra V, Ayas C, Langelaar M, Van Keulen F. Simultaneous topology and deposition direction optimization for Wire and Arc Additive Manufacturing. Manuf Lett 2022;31:45–51.
[16] Laghi V, Palermo M, Bruggi M, Gasparini G, Trombetti T. Blended structural optimization for wire-and-arc additively manufactured beams. Prog Addit Manuf 2023;8(3):381–92.
[17] Kokare S, Oliveira JP, Santos TG, Godina R. Environmental and economic assessment of a steel wall fabricated by wire-based directed energy deposition. Addit Manuf 2023;61:103316.
[18] Kelly JM, Skinner RI, Heine AJ. Mechanisms of energy absorption in special devices for use in earthquake resistant structures. Bull NZ Soc Earthq Eng 1972;5(3):63–88.
[19] Roeder CW, Popov EP. Eccentrically braced steel frames for earthquakes. J Struct Div 1978;104(3):391–412.
[20] Aziz I, Amanat KM. Equivalence of plastic strength and hysteretic behavior of box and I-shaped shear links. Structures 2022;Vol. 40:356–69. https://doi.org/10.1016/j.istruc.2022.04.012.
[21] Ghadami A, Pourmoosavi GH. Numerical investigation on the flange contribution in the shear strength of short LYP I-shaped links without intermediate stiffeners. Structures 2022;Vol. 40:485–97. https://doi.org/10.1016/j.istruc.2022.04.043.
[22] Lázaro L, Chacón R. Influence of the designer-assumed cyclic hardening parameters on the overstrength of austenitic stainless-steel links. Thin-Walled Struct 2023;190:111015.
[23] Roy SC, Goyal S, Sandhya R, Ray SK. Low cycle fatigue life prediction of 316 L (N) stainless steel based on cyclic elasto-plastic response. Nucl Eng Des 2012;253:219–25.
[24] Mazánová V, Škorík V, Kruml T, Polák J. Cyclic response and early damage evolution in multiaxial cyclic loading of 316L austenitic steel. Int J Fatigue 2017;100:466–76.
[25] Eng MBPD, Uang CM, SE RS. Ductile design of steel structures. McGraw-Hill Education,; 2011.
[26] Lian M, Su M. Seismic performance of high-strength steel fabricated eccentrically braced frame with vertical shear link. J Constr Steel Res 2017;137:262–85.
[27] Liu XG, Fan JS, Liu YF, Yue QR, Nie JG. Experimental research of replaceable Q345GJ steel shear links considering cyclic buckling and plastic overstrength. J Constr Steel Res 2017;134:160–79.
[28] Ramonell C, Chacon R. On the topological optimization of horizontal links in eccentrically braced frames. J Constr Steel Res 2021;185:106887.
[29] Cheng Q, Lian M, Su M, Zhang H. Experimental and finite element study of high-strength steel framed-tube structures with replaceable shear links under cyclic loading. Structures 2021;Vol. 29:48–64. https://doi.org/10.1016/j.istruc.2020.11.006.
[30] Men J, Xiong L, Wang J, Zhang Q, He P. An experimental study on the seismic behavior and replaceability of the replaceable steel shear links. *Structures* 2021;Vol. 33:2334–48. https://doi.org/10.1016/j.istruc.2021.05.075.
[31] ABAQUS. Version 2019. Pawtucket, USA: Hibbitt, Karlsson & Sorensen, Inc.; 2019.
[32] Liu XG, Liu YF. Cyclic behavior of Q345GJ steel used in energy dissipation shear links. Int J Steel Struct 2016;16:697–704.
[33] Sigmund O, Maute K. Topology optimization approaches: a comparative review. Struct Multidiscip Optim 2013;48(6):1031–55.
[34] Bendsoe MP, Sigmund O. Topology optimization: theory, methods, and applications. Springer Science & Business Media,; 2013. https://doi.org/10.1007/978-3-662-05086-6.
[35] Bendsøe MP, Sigmund O. Material interpolation schemes in topology optimization. Arch Appl Mech 1999;69:635–54.
[36] Diegel O, Nordin A, Motte D. A practical guide to design for additive manufacturing. Singapore: Springer Singapore,; 2019. p. 978–81.
[37] Wijesundara KK, Nascimbene R, Sullivan TJ. Equivalent viscous damping for steel concentrically braced frame structures. Bull Earthq Eng 2011;9:1535–58.
[38] AISC (American Institute of Steel Construction). Seismic provisions for structural steel buildings. ANSI/AISC 341–16, Chicago, IL; 2016.